

# 1 A new electrodynamic balance design for low temperature 2 studies

3

4 H.-J. Tong<sup>1</sup>, B. Ouyang<sup>1</sup>, N. Nikolovski<sup>2</sup>, D. M. Lienhard<sup>1</sup>, F. D. Pope<sup>3\*</sup> and M.  
5 Kalberer<sup>1</sup>

6

7 [1]{Centre for Atmospheric Science, University of Cambridge, Lensfield Road, Cambridge,  
8 CB2 1EW, United Kingdom}

9 [2]{Department of Biochemistry, University of Cambridge, Tennis Court Road, Cambridge,  
10 CB2 1QW, United Kingdom}

11 [3]{School of Geography, Earth and Environmental Sciences, University of Birmingham,  
12 Edgbaston, Birmingham, B15 2TT, United Kingdom}

13 Correspondence to: F. D. Pope (f.pope@bham.ac.uk)

14

## 15 Abstract

16 In this paper we describe a newly designed cold electrodynamic balance (CEDB) system,  
17 built to study the evaporation kinetics and freezing properties of supercooled water droplets.  
18 The temperature of the CEDB chamber at the location of the levitated water droplet can be  
19 controlled in the range: -40 °C to +40 °C, which is achieved using a combination of liquid  
20 nitrogen cooling and heating by positive temperature coefficient heaters. The measurement of  
21 liquid droplet radius is obtained by analysing the Mie elastic light scattering from a 532 nm  
22 laser. The Mie scattering signal was also used to characterize and distinguish droplet freezing  
23 events; liquid droplets produce a regular fringe pattern whilst the pattern from frozen particles  
24 is irregular. The evaporation rate of singly levitated water droplets was calculated from time  
25 resolved measurements of the radii of evaporating droplets and a clear trend of the  
26 evaporation rate on temperature was measured. The statistical freezing probabilities of  
27 aqueous pollen extracts (pollen washing water) are obtained in the temperature range: -4.5 to -  
28 40 °C. It was found that that pollen washing water from water birch (*Betula fontinalis*

1 *occidentalis*) pollen can act as ice nuclei in the immersion freezing mode at temperatures as  
2 warm as  $-22.45 (\pm 0.65) ^\circ\text{C}$ . Furthermore it was found that the protein rich component of the  
3 washing water was significantly more ice active than the non-proteinaceous component.  
4

## 5 **1 Introduction**

6 At sub-zero temperatures, water is observed in clouds as both supercooled water droplets  
7 (SWD) and ice particles (Mason, 1975; Cantrell and Heymsfield, 2005). In the absence of ice  
8 nuclei (IN), cloud droplets can be supercooled down to temperatures that approach the  
9 homogeneous freezing point  $\sim -38^\circ\text{C}$  which is dependent on droplet size (Sassen, 1985;  
10 Rauber and Tokay, 1991; Hogan et al., 2004). The evaporation kinetics, and hence droplet  
11 size, of SWD influences the lifetime and radiative properties of clouds and in particular  
12 mixed-phase clouds; it can also affect the likelihood and rate of precipitation (Rosenfeld and  
13 Woodley, 2000; Lohmann and Feichter, 2005).

14 At temperatures above the homogenous freezing point, the heterogeneous freezing of SWD is  
15 caused by interaction of IN active aerosols with SWD. Several distinct mechanisms exist,  
16 including: the deposition, immersion, condensation, and contact modes of freezing (Prupacher  
17 and Klett, 1997). Recently there has been an intense research effort to determine the  
18 efficiencies and relevance of the different modes of freezing (e.g. Murray et al., 2010; Knopf  
19 et al., 2011; Crawford et al., 2011; Kanji et al., 2013; Hoffmann et al., 2013; Atkinson et al.,  
20 2013.) Summaries of previous results, obtained by both laboratory and field work, and the  
21 atmospheric implications of these studies are provided by several recent review articles and  
22 no further detail is given here (Laaksonen et al, 1995; Pöschl, 2005; Hoose and Möhler, 2012;  
23 Murray et al., 2012; Ladino Moreno et al., 2013). It is noted that several studies suggest that  
24 IN processes are still not sufficiently understood for satisfactory global modelling (e.g. Hoose  
25 et al., 2010; DeMott et al., 2010). The most important types of aerosol particles to act as IN  
26 are reported to be mineral dust and primary biological aerosols (PBA), with these two aerosol  
27 groups accounting for more than 80 % of ice-crystal residues (Pratt et al., 2009). PBA are  
28 typically large in size (mainly supermicron) and they often dominate the measured mass  
29 loading of atmospheric aerosol. However, their number density concentration is small and  
30 usually dwarfed by other aerosol types except in the most pristine environments (Griffiths et  
31 al., 2012). PBA species include: pollen, bacteria, fungal, algae, moss and fern spores, viruses  
32 and fragments of animals and plants (Deguillaume et al., 2008, Moller et al., 2008, Després et

1 al., 2007, Möhler et al., 2007). The atmospheric transport, and hence dispersal, of pollen  
2 requires meteorological conditions to produce uplift of pollen containing air. Atmospheric  
3 removal of pollen is determined by the wet and dry deposition rates. The dry deposition is  
4 controlled by the settling speed of the pollen grain which is a function of particle density and  
5 size (Aylor 2002). Both computer modelling and field studies have shown that pollen is  
6 capable of travelling large distances and can remain airborne on the order of days (Rousseau  
7 et al., 2003, Sofiev et al., 2006, Helbig et al., 2004, Heise and Heise 1948).

8 Previous work in our group has used the environmental scanning electron microscope (ESEM)  
9 and warm EDB systems to measure the hygroscopicity and hence the warm cloud  
10 condensation nuclei (CCN) ability of pollen grains (Pope 2010; Griffiths et al., 2012). Within  
11 liquid water, such as in rain droplets, pollen grains are observed to burst thereby releasing  
12 smaller material, such as sugars, macromolecules and allergens, into solution (Yttri et al.,  
13 2007; Schäppi et al., 1999; Pummer et al., 2012; Augustin et al., 2013).

14 Pollen grains have been found to be IN active. Within the condensation freezing mode pollen  
15 can initiate freezing events at temperatures up to  $-8\text{ }^{\circ}\text{C}$  (Diehl et al., 2001), within the  
16 immersion freezing mode at temperatures up to  $-9\text{ }^{\circ}\text{C}$  (Diehl et al., 2002), and within the  
17 contact freezing mode up to  $-5\text{ }^{\circ}\text{C}$  (Diehl et al., 2002). Furthermore, it is found that water that  
18 has interacted with pollen grains can also be IN active in the immersion mode of freezing.  
19 This water is referred to as pollen washing water (PWW). In particular, suspended  
20 macromolecules within PWW were identified as efficient IN (Pummer et al., 2012; Augustin  
21 et al., 2013). Work by the group of Grothe has used two distinct techniques to assess the IN  
22 ability of PWW ensembles: firstly freezing events of PWW droplets that are held within  
23 emulsions can be observed through use of a microscope fitted with a cryostage (Pummer et al.,  
24 2012). Secondly the Leipzig Aerosol Cloud Interaction Simulator (LACIS, Stratman et al.;  
25 2004) technique is utilized (Augustin et al., 2013). These results strongly indicate the high IN  
26 efficiency of PWW in immersion mode up to  $-16\text{ }^{\circ}\text{C}$ .

27 As a robust methodology for the levitation of single particles which carry electric charge, the  
28 electrodynamic balance (EDB) technique has been applied in atmosphere science for several  
29 decades (see reviews by Davis, 1997; Krieger et al., 2012). On the base of such a strategy,  
30 numerous work has been carried out on aerosol particles and droplets, including but not  
31 limited to: contact ion pairs formation (e.g. Zhang and Chan, 2000; Lee et al., 2008),  
32 hygroscopicity and phase transition (e.g. Tang and Munkelwitz, 1994; Choi and Chan, 2002;

1 Li et al., 2005; Parsons et al., 2006; Pope et al., 2010a), measurement of vapour pressure (e.g.  
2 Pope et al., 2010b, Soonsin et al., 2010), oxidation chemistry (e.g. Lee and Chan, 2007; Pope  
3 et al., 2010c; Lee et al. 2012), and supercooled droplets and ice nucleation (e.g. Swanson et  
4 al., 1999; Krieger et al., 2000; Svensson et al., 2009; Hoffmann et al., 2013a; Hoffmann et al.,  
5 2013b). Recently, a new EDB design with concentric cylindrical electrodes was developed  
6 to measure rapid evaporation and condensation process of single droplets (Heinisch et al.,  
7 2006, 2009; Davies et al., 2011, 2013).

8 Using a similar EDB design to Heinisch et al., we developed and incorporated a new cooling  
9 system which is applicable for low temperature studies. The Heinisch design was chosen  
10 because the cylindrical electrodes are mechanically stable and single droplets can be stably  
11 confined within a small and well defined null point region of the electrodynamic balance  
12 whilst gas flows (>100 sccm) are directed past the droplet (Heinisch et al., 2006; Davies et al.,  
13 2011). We describe the new cold EDB (CEDB) system providing particular detail on the  
14 cooling strategy. Furthermore, we provide measurement data, from the first applications of  
15 this new system: the evaporation rates of supercooled droplets, and the freezing ability of  
16 these droplets with and without PWW present. In particular this study provides the first  
17 contact free measurements of ice nucleation of individual PWW droplets.

18

## 19 **2 Design and characterisation of new CEDB**

20 The schematic diagram of the new CEDB system is shown in Figure 1. The system is capable  
21 of trapping droplets and following the evolution of the droplet radius under well-defined  
22 conditions of temperature and humidity. Evaporation and freezing of droplets are  
23 distinguished by following the Mie scattering phase function. The detailed experimental  
24 procedure and analysis strategy is detailed.

25

### 26 **2.1 Droplet Trapping and Sizing**

27 The details of the geometrical structure of the EDB chamber, AC and DC electrodes, and the  
28 theoretical calculation on the electrodynamic field generated have been reported previously by  
29 Heinisch et al. (2009) and Davies et al., (2012) and will be discussed only briefly here. The  
30 outer surface of the alumina CEDB chamber body has octagonal geometry with an optical

1 port window situated on each flat surface. BK7 glass lenses (Knight Optical, 13 mm in  
2 diameter) are mounted in each window to allow passage of light into and out of the chamber.  
3 The inner surface of the CEDB chamber has cylindrical geometry with an internal volume of  
4 approximately 45.6 cm<sup>3</sup>.

6 As shown in Figure 1, the cylindrical electrodes are composed of two inner (cyan colour, ①)  
7 and two outer (yellow colour, ②) copper electrodes. The inner electrodes are 10 mm long  
8 and an inner diameter of 2 mm. The inner diameter (for the open) and length of the outer  
9 electrodes are 8 mm and 13 mm respectively. The outer electrodes are directly mounted on  
10 the stainless steel base of the CEDB chamber and grounded. The inner electrodes are also  
11 mounted on CEDB bases. However, the inner electrodes are electrically insulated from the  
12 outer electrodes as well as the metal bases by using a 1 mm thick rubber insulator. After  
13 stable mounting of the 4 electrodes, the distances between the upper and lower electrodes are  
14 8 mm for the inner electrodes and 4 mm for the outer electrodes.

16 The combined DC and AC electric field ( $V_{AC}+V_{DC}$ ) is generated using Labview software, that  
17 is transferred through a digital-to-analog converter and amplified using a high speed and high  
18 voltage amplifier module (AP-1B3, Matsusada Precision Inc.). The DC voltage applied to  
19 upper inner electrode can be varied between -200 – 0 V, the AC voltage between 0 – 1 kV,  
20 and the AC frequency between 10 – 300 Hz. The lower-inner electrode has the same AC input  
21 applied to it as the upper-inner electrode but without the DC coupling.

23 Droplets were delivered into the CEDB using a droplet dispenser, which is optimized for low  
24 temperature conditions, (MicroFab, 30 (MJ-ABP-01) or 100 (MJ-AB-01)  $\mu\text{m}$  orifice  
25 diameter). When the same dispenser parameter settings (pulse width, frequency and  
26 amplitude etc.) are used the generated droplets are of high reproducibility with radius  
27 fluctuation smaller than 0.5  $\mu\text{m}$ . Within this study the use of different parameter settings led  
28 to slight differences in initial SWD size. From the dispenser the droplets follow a trajectory  
29 past a charging electrode which is held at 900 V (generated from a Brandenburg 476R high  
30 voltage photomultiplier power supply) thereby allowing the droplet to pick up sufficient  
31 charge for trapping. Subsequent to the charging electrode, the droplets pass into the centre of

1 the CEDB chamber where the droplets are trapped in the null point of the electrodynamic  
2 field.

3 The procedure for the size calibration of the droplet is the same as we previously used (Pope  
4 et al., 2010b). A cw 532 nm wavelength laser (532GLM20, Changchun Dragon Lasers Co.,  
5 Ltd), with a power of ~ 20 mW, illuminates the trapped spherical droplet thus generating Mie  
6 scattering resonances. These resonances were recorded over a 21° window, as measured by  
7 the angle subtended from the null point to the edges of the window port, using a monochrome  
8 complementary metal oxide semiconductor camera (Thorlabs, DCC1545M) centred at ~135°  
9 relative to the forward direction of the laser. The particle size obtained by Mie scattering was  
10 calibrated using dry lime soda glass sphere standards of the following diameters: 19.3±1.0,  
11 30.1±1.1, 42.3±1.0 µm (Thermo Scientific Duke Standards, 9020, 9030, 9040). Thousands of  
12 Lime soda spheres are transformed from stock vial into a syringe needle first. Then the needle  
13 containing the spheres is connected with a syringe which is full of air. Continually the spheres  
14 are injected into the CEDB chamber by squeezing the air out from the syringe in less than  
15 1second. Once a particle is trapped, the Mie scattering function is recorded automatically by  
16 the camera. Afterwards, the calculated result based on equation (1) (Glantschnig and Chen,  
17 1981), which is based on Mie theory (Mie 1908), will be compared to the experimentally  
18 determined peak-to-peak average of the recorded resonances. The position of the camera for  
19 collecting the Mie scattering signal is optimized according to the standard deviation of the  
20 theoretical and experimental values. The excellent agreement between the experimental  
21 calibration data and the theoretical calculations are shown in Figure 2. Labview 11 software  
22 was used for experimental control and data acquisition.

23

24

25

$$\Delta\theta \cong \frac{\lambda}{r} \left( \cos \frac{\theta}{2} + \frac{n \sin \frac{\theta}{2}}{\sqrt{1+n^2-2n \cos \frac{\theta}{2}}} \right)^{-1} \quad (1)$$

26

27 In equation (1)  $\lambda$  is the illuminating laser wavelength (532 nm).  $n$  is the refractive index of  
28 trapped droplet (the value of 1.33 will be used in this study for pure water),  $\theta$  is the median  
29 angle of observed phase functions, and  $\Delta\theta$  is the angular separation.

1 We have characterized the trapping ability of CEDB under three different flow regimes:

2 (i) stagnant conditions with no gas flow through the electrodes provide the most stable  
3 trapping. As no downward force from the gas flow though the CEDB is present, a particle  
4 can be trapped (by a symmetric electrical field) in a short time with a high trapping success  
5 rate. In addition it is observed that the particle can be moved up and down by the DC voltage  
6 freely under stagnant conditions. Whilst stagnant conditions produced conditions beneficial  
7 to stable trapping, trapping temperatures lower than  $< -30\text{ }^{\circ}\text{C}$  could not be achieved. Hence  
8 further experiments were not performed under stagnant conditions because temperatures as  
9 low as the homogenous freezing temperature were required for the experiments described  
10 below.

11 (ii) When gas is flowing through both cooling lines (controlled by MFC 1 and 2 in Figure 1a)  
12 a relatively large cross sectional area of ca.  $50\text{ mm}^2$  of near constant gas flow velocity is  
13 generated within the CEDB. This uniform flow facilitates the stable trapping of particles over  
14 long time scales as they experience the same flow forces regardless of small radial oscillations  
15 which can occur within the CEDB due to the changing size of the particle during an  
16 experiment. Flow rates of 50 sccm and 200 sccm for the inner flow and outer flow,  
17 respectively, provide such stable conditions.

18 (iii) The least stable trapping conditions were found when gas was only passed through the  
19 inner electrode as this resulted in a much smaller cross sectional area (ca.  $3\text{mm}^2$ ) with uniform  
20 flow conditions. Consequently only flow rates up to 10sccm could be used in this  
21 configuration.

22

## 23 **2.2 Cooling Strategy of CEDB**

24 To cool the CEDB system, a 300 mm long and 50 mm inner diameter vacuum insulated liquid  
25 nitrogen Dewar was attached to the top of the CEDB. This Dewar consists of double walled  
26 liquid nitrogen steel reservoir with a vacuum held between the two walls. The thickness of the  
27 Dewar wall and vacuum layer are larger than 1 and 5 mm, respectively. To further reduce heat  
28 exchange between the liquid nitrogen Dewar and the ambient atmosphere, the outer surface of  
29 the liquid nitrogen cylinder is covered with flexible synthetic rubber insulation (Insul-tube  
30 and Insul-sheet, NMC (UK) Ltd) with a thickness of  $\sim 9$  mm. The top of the Dewar is sealed  
31 with a Polytetrafluoroethene (PTFE) cap which is also insulated with synthetic rubber. The

1 vacuum and insulation material significantly reduce the evaporation of liquid nitrogen.  
2 Additionally, the liquid nitrogen is refilled periodically thereby increasing the temperature  
3 stability within the CEDB chamber (fluctuation is <0.2 °C after equilibrium).

4 The CEDB chamber is cooled by flowing N<sub>2</sub> gas through two copper heat exchange tubes (3  
5 mm outside diameter). The pipes pass through the liquid nitrogen Dewar and direct the gas  
6 flows through the upper electrodes (see Figure 1). The gas flow from the central pipe passes  
7 through the upper-inner electrode and directly passes through the null point region of the  
8 CEDB. The gas flow from the outer pipe is directed through the gap formed between the inner  
9 and outer-upper electrodes and acts as an additional cooling sheath gas as described above.  
10 The gas flows are controlled using mass flow controllers (Brooks Smart MFC, Brooks  
11 Instruments) and are normally set to ~80 sccm for the outer pipe (MFC 1 in Figure 1) and 20  
12 sccm for the central pipe (MFC 2 in Figure 1). These flow rates are both laminar and matched  
13 in downward velocity. The Reynolds number of the two gas flows, can be calculated with  
14 equation (2), where  $d$  is diameter of inner (0.002 m) or outer electrode (0.004 m).  $u$  is the  
15 mass flow velocity (m/s).  $\rho$  is the density (1.13 kg/m<sup>3</sup> for nitrogen gas).  $\eta$  is the dynamic  
16 viscosity (1.75×10<sup>-5</sup> pa·s for nitrogen gas at 20 °C). The calculated Reynolds numbers at 20  
17 °C are 27.4 and 13.7 for the 80 and 20 sccm flow rates, respectively. These low Reynolds  
18 numbers comfortably ensure laminar flow at all temperatures investigated in this study.

19

20

21

$$\text{Re} = \frac{du\rho}{\eta} \quad (2)$$

22

23 The temperature at the null point of the CEDB is controlled by varying the temperature of the  
24 CEDB chamber wall using variable heaters (HP05-1/10-24, Onecall). The null point  
25 temperature and radial temperature gradient are measured using a 0.1 °C resolution  
26 thermometer (HH 308, Omega) with type K thermocouples. A temperature calibration curve  
27 for the null point position is shown in Figure 3a. It can be seen that the null point temperature  
28 varies linearly with the DC voltage that is supplied to the heater. This configuration allows for  
29 easy control of the null point temperature between -40 – 0 °C. When insulating all the 8 outer  
30 metal surfaces of the CEDB chamber with 4 mm depth rubber insulator, the null point



1 temperature can be controlled from -30 to -42 °C with a heating range from 17 to 38 V. If  
2 only 6 outer metal surfaces are insulated, the null point temperature can be regulated from 40  
3 to -31 °C with a heating range from 24 to 43 V. Only the calibration curve ranges from 5 to -  
4 42 °C are shown in Figure 3. This configuration sets up a radial temperature gradient within  
5 the cell at the height of the null point. As a result of the diffusional mixing of the cold and  
6 warm gases, upstream of the null point will be colder than downstream, the null point  
7 temperature will be at an intermediate temperature. The temperature gradients were measured  
8 by accurately positioning a thermocouple (5SC-GG-(K)-30-(36), max  $\pm 2.2$  °C) in the cell, are  
9 shown in table 1 for five temperatures at the null point from -5 °C to -42 °C. Although the  
10 maximal accuracy of the thermocouple is  $\pm 2.2$  °C, we also calibrated with a TSP01-USB  
11 Temperature and Humidity sensor ( $\pm 0.5$  °C Thorlabs) in the temperature range -15 to 25 °C.  
12 The difference of the two kind of sensor is smaller than 0.1 °C in the whole range.  
13 Additionally, temperature of the liquid nitrogen is observed to be -194 °C with the K type  
14 thermocouple, which is quite close to the boiling point of liquid nitrogen (Haynes 2013).  
15 Hence we suggest the thermocouple we used is reliable. Temperature gradients in the axial  
16 directions (above and below the null point) were  $< 3$  °C/mm and radial gradients of  $< 1$  °C  
17 were measured throughout the temperature range. During the experiment, the trapped particles  
18 are always confined at the null point ( $\pm 1$  mm) by adjusting controlling AC or DC parameters  
19 with the feedback program with in the Labview (as discussed in section 2.1). Thus, we are  
20 confident that the trapped particle will not deviate significantly in any direction from the null  
21 point.

22 The relative humidity (RH) at the null point can get  $< 0.2$  % (EK-H5 kit with SHT75  
23 Humidity sensor, Sensirion) when the temperature is higher than -20 °C, and  $< 0.7$  % when the  
24 temperature reaches  $\sim -40$  °C. The standard RH deviation of the SHT75 probe is  $\sim \pm 4\%$  at 0%  
25 RH. Figure 3b provides an example of the time required for the temperature of both the  
26 CEDB null point and the outer glass window surface to reach steady state.

27 The current instrument design only allows performing experiments at low RH due to the gas  
28 flow passing through the liquid nitrogen reservoir. Higher RH conditions in the CEDB could  
29 be reached by cooling the copper tubes less either by insulating the copper tubes in the liquid  
30 nitrogen reservoir or by using higher temperature coolants or by introducing a separate  
31 humidified gas flow. The capability to adjust the RH will be integrated in the next version of  
32 our CEDB.

1 In order to stop the formation of condensation and or freezing on the outer surface of the glass  
2 windows, a rubber insulator (⑥ in Figure 1) was used between the window and metal body  
3 of the chamber. Furthermore, the outer surface of the glass window was warmed by a heating  
4 jacket (④ in Figure 1). The jacket was designed so the outside face of the window could be  
5 exposed to the laboratory air. Such a design allows for the easy alignment of the laser into the  
6 chamber and through the CEDB null point. When the outside surface temperature of the glass  
7 windows was lower than 15 °C, a dry laminar air flow is also directed onto the surface to  
8 avoid water condensation and to maintain the transparency of the window.

9 In order to quantify the CEDB temperature for low temperature application, we observed the  
10 homogeneous ice nucleation of pure supercooled water droplets. We found the Mie scattering  
11 pattern of SWD become highly irregular at  $-38\pm 1^\circ\text{C}$ , see example data in Figure 2b, which  
12 corresponds to the homogeneous ice nucleation of SWD. This is in good agreement with  
13 established literature value (Koop et al. 2000).

14

### 15 **3 Results and discussion**

16 The first applications of the new CEDB system, detailed in this paper, are in the study of the  
17 evaporation kinetics of SWD and the immersion freezing ability of PWW droplets.

18

#### 19 **3.1 Evaporation kinetics of supercooled water droplets**

20 As the main application of the CEDB, in this paper, will be the investigation of freezing  
21 events of aqueous droplets it is necessary to characterise the evaporation rate of SWD, which  
22 defines the time window accessible for the freezing studies.

23 The mean free path of  $\text{N}_2$  gas ( $\lambda_{\text{N}_2}$ ) at sub-zero temperatures and atmospheric pressure is less  
24 than 58.8 nm (Hirschfelder et al., 1954). Considering that the measured droplet radius ( $r$ ) is  
25 always greater than  $2.5\ \mu\text{m}$ , then the Knudsen number,  $\text{Kn} = \lambda_{\text{N}_2}/r$ , is always much smaller  
26 than 1 therefore the  $\text{N}_2$  gas flow is always in the continuum regime (Seinfeld and Pandis,  
27 1998). Hence both the mass transfer of water molecules from the SWD surface to the  
28 surrounding  $\text{N}_2$  atmosphere as well as the heat transfer is significant in influencing the kinetic  
29 evaporation rate of the trapped SWDs (Miles et al., 2012; Holyst et al., 2013). Due to the  
30 influence of heat transfer, the surface temperature of SWD will be lower than the surrounding

1 gas flow and this reduces the observed evaporation rate. It is noted that under dry conditions  
2 such as in our setup, the colder the surrounding gas flow, the smaller the temperature  
3 difference between the droplet surface and the gas phase (Kulmala et al. 1993; Miles et al.  
4 2012). The gas flow rate through the CEDB chamber can influence the evaporation rate due to  
5 the effects of Stefan flow (Davies et al. 2014), however this effect is calculated to be  
6 negligible in the CEDB system, and will not be discussed further here.

7  
8 To ensure that the nitrogen gas was as dry as possible, the flow from the cylinder was passed  
9 through a 300 mm long, and 50 mm in diameter, drying tube containing silica gel particles  
10 (Breckland Scientific Supplies Ltd). Any remaining water vapour in the gas flow is caught in  
11 the cold trap formed by copper tubing heat exchangers which are held at near liquid nitrogen  
12 temperature (-196 °C). Considering the saturation vapour pressures of liquid water and ice at  
13 ~ -150 °C (123 K) are  $3.02 \times 10^{-9}$  and  $8.50 \times 10^{-10}$  Pa, and the vapour pressure is decreasing as  
14 the temperature is lowering (Murphy and Koop, 2005), we assume that the evaporation of  
15 SWD in the present study occurs under a dry environment. HPLC grade water (RH1020,  
16 Rathburn Chemicals Ltd.) was used to generate the water droplets. Pure water droplets were  
17 only injected into the CEDB chamber once the null point temperature had stabilized to the  
18 desired temperature.

19  
20 The evaporation rate of SWD recorded at -18.8 ( $\pm 0.6$ ), -22.7 ( $\pm 0.6$ ), -28.0 ( $\pm 0.6$ ), -32.1 ( $\pm 0.6$ )  
21 and -34.2 ( $\pm 0.6$ ) °C, as measured by the change in radius, are shown in Figure 4 (a). This  
22 figure indicates that under dry nitrogen gas flow the evaporation rate of SWD decreases as  
23 temperature of the null point decreases, as expected, because of the decreasing water vapour  
24 pressure. The evaporation rate of SWD can be parameterized by determining the time taken  
25 for the droplet to evaporate to half of its initial radius ( $t_{r1/2}$ ). As expected it is observed that  
26 the evaporation rates of SWDs increase with the initial size of the SWD because of the greater  
27 number of water molecules transferred from liquid to gas phase. An alternative  
28 parameterization is the ratio of  $t_{r1/2}$  to the initial radius of the droplet ( $t_{r1/2}/R$ ) is used to  
29 minimise the influence of initial SWD size as shown in Figure 4 (b). This parameterization  
30 strategy has been previously used as an empirical tool to estimate the mass transfer of water  
31 molecules in glassy aerosol droplets (Tong et al., 2011).

1 Although in this study we do not quantify the influence of mass and heat transfer on the  
2 evaporating rate of SWDs, these results show that SWD evaporation kinetics can be measured  
3 using the new CEDB design described in this paper, at temperatures as low as the  
4 homogenous freezing temperature. This study will form the basis of a forthcoming paper.

5  
6 Importantly for the upcoming discussion on heterogeneous freezing, we conclusively  
7 demonstrate that water droplets with an initial radius of  $\sim 15 \mu\text{m}$  can be trapped for ca. 10 –  
8 60 s within a  $\sim 100$  sccm pure nitrogen gas in the temperature range from  $-5.7$  to  $-34.5 \text{ }^\circ\text{C}$ , thus  
9 defining the time scale available for freezing experiments in the current CEDB set up.

### 11 3.2 Immersion Freezing of PWW Solution

12 The extraction procedure for the PWW solutions, which is illustrated in Figure 5a, is similar  
13 to the procedure used by Augustin et al. (2013). Briefly, water birch pollen (*Betula fontinalis*  
14 *occidentalis*), which was obtained as a dried sample from Sigma-Aldrich (P6895-1G), were  
15 suspended in water at a mass concentration of 5 g/ml and stirred for  $\sim 1$  minute using a mixer  
16 (Fisher Scientific Top Mix FB 15024). After stirring, the suspension was then stored in a  
17 fridge for 24 hours. The solution was then stirred again and filtered through sequential use of  
18  $0.45$  and  $0.2 \mu\text{m}$  pore filters (Supelco, 4 mm, PTFE membrane). In this aspect the procedure  
19 differed from that of Augustin et al. which used filters of size  $4 - 7 \mu\text{m}$ . After the filtration,  
20 the PWW solution is observed to be transparent but with a bright yellow hue. Each filtered  
21 PWW solution was used within 4 days of preparation to minimize the risk of contamination.  
22 The mass fraction ( $f_{\text{PWW}}$ ) of biological material within the PWW solution is obtained by  
23 measuring the mass of the extracted PWW solution and mass of the dried residue with a  $0.1$   
24 mg accuracy balance (Fisherbrand PS-60). Dry PWW residues were obtained by evaporating  
25 the PWW solutions under nitrogen gas (Air liquid UK limited,  $>99.999\%$ ) and subsequent  
26 heating within an oven (Memmert, ULM 400) at a temperature  $< 95 \text{ }^\circ\text{C}$  for more than 4 hours.

27 Figure 6 provides the calibration curve for the mass fraction of biological material in solution  
28 versus initial concentration of pollen mass in the extraction solution. Furthermore, the  
29 refractive index of the PWW solution is measured using a refractometer (RFM340,  
30 Bellingham + Stanley Ltd.), also shown in Figure 6. Figure 6 clearly indicates that the mass  
31 fraction of PWW solutions ( $f_{\text{PWW}}$ ) increase from  $0.000135 - 0.0129$  as the pollen suspension

1 concentration ( $W_{\text{pollen}}$ ) increases from 1 – 50 mg/ml (pollen mass per water volume). The  
2 upper threshold,  $f_{\text{PWW}} = 0.0129$ , in this study is similar to mass fractions used in the study of  
3 Pummer et al. (2012). However, within the experiments described in this study, the values of  
4  $f_{\text{PWW}}$  will increase as the water content of the PWW droplets evaporate. The refractive index  
5 of PWW solutions ( $RI_{\text{PWW}}$ ) increase from 1.332905 (pure water) to 1.33543 as the pollen  
6 suspension concentration increase from 0 to 50 mg/ml. To calculate the particle size, via  
7 equation E2, we used the refractive index value of pure water ( $n = 1.33$ ) in all cases. For a 15  
8  $\mu\text{m}$  (in radius) PWW droplet, without considering the density evolution of it during the  
9 evaporation process, at most this simplification led to an overestimation of the initial droplet  
10 size by  $\sim 0.28\%$ , and  $0.54\%$  for the same droplet at time  $t_{1/2}$ .

11 Freezing events of the PWW droplets are identified by the change in the elastic Mie scattering  
12 signal. Liquid droplets are spherical and produce regular fringe patterns, whilst frozen solid  
13 particles are non-spherical and produce irregular patterns. Such a strategy for distinguishing  
14 liquid and frozen droplets has been successfully demonstrated previously (e.g. Krämer et al.,  
15 1999; Shaw et al., 1999; Vortisch et al., 2000). Examples of different phase functions are  
16 shown in Figure 5 panels b, c, d, and e. In particular, Figure 5b provides images of scattered  
17 light recorded at 1.3 and 10 s, respectively, after capture in the EDB trap from a PWW droplet  
18 at  $-21.8\text{ }^\circ\text{C}$ ; the reduction in fringe spacing clearly indicates that the droplet has lost some of  
19 its water content through evaporation but has not frozen. Figure 5c provides images of the  
20 scattered light recorded immediately after trapping (0.0 s) and 5.0 s after injection for a frozen  
21 PWW droplet at  $-24.2\text{ }^\circ\text{C}$ , both phase functions are irregular indicating that this droplet was  
22 frozen almost instantaneously within the trap. Figure 5d shows the phase functions of a  
23 trapped PWW 0.4 and 2.6 s after injection; the first phase function is regular and the second is  
24 irregular indicating that a freezing event happened after a short period of evaporation. Figure  
25 5e provides the phase functions, at 0 and 60 s after injection, for a PWW which freezes  
26 instantaneously at  $-32.2\text{ }^\circ\text{C}$ .

27 To test the freezing efficiency of PWW solution droplets, experiments were performed at ten  
28 different temperatures. The temperature dependent freezing fractions ( $f_{\text{ice}}$ ) of the PWW  
29 droplets, is calculated using equation 3.

30

31 
$$f_{\text{ice}} = \frac{N_f}{N_0} \quad (3)$$

1 Where  $N_f$  is the number of PWW droplets that freeze, and  $N_0$  is the total number of PWW  
2 droplets. 30-158 droplets were analysed at each temperature (as shown in Figure 7). At the  
3 highest and lowest temperatures fewer droplets were required for good statistics. A greater  
4 number of droplets were measured in the temperature region where the value of  $f_{ice}$  is  
5 evolving rapidly. The numbers of PWW droplets used were: 158 for  $-15.2 (\pm 0.7) ^\circ\text{C}$ , 82 for  $-$   
6  $18.8 (\pm 0.85) ^\circ\text{C}$ , 151 for  $-20.5 (\pm 0.65) ^\circ\text{C}$ , 104 for  $-22.5 (\pm 0.65) ^\circ\text{C}$ , 125 for  $-24.2 (\pm 0.65) ^\circ\text{C}$ ,  
7 100 for  $-27.5 (\pm 0.5) ^\circ\text{C}$ , 50 for  $-30.5 (\pm 0.5) ^\circ\text{C}$ , and 60 for  $-32.2 (\pm 0.5) ^\circ\text{C}$ .

8 The ice freezing fraction of droplets initially generated from 5 and 47 mg/ml PWW solution is  
9 shown in Figure 7. It is noted that the PWW droplet surface temperature will be lowered with  
10 the heat transfer effect. As the droplet water evaporates the concentration of the non-volatile  
11 biomaterial within droplet will become more concentrated. However, in droplets where  
12 freezing was observed, the freezing occurred within 0.3 seconds after injection of the PWW  
13 droplets into the trap. In this short time window the droplets do not evaporate significantly,  
14 see Figure 4a. In a very small number of PWW droplets (<5%) freezing occurred after 0.3  
15 seconds but these droplets were not considered in the data analysis shown in Figure 7 and 8.

16

17 A clear increasing trend for  $f_{ice}$  was observed with decreasing temperature for both the 5 and  
18 47 mg/ml PWW solution droplets, see Figure 7. For the 5 mg/ml PWW, the  $f_{ice}$  increases  
19 rapidly from 0 to 0.85 as the temperature is lowered from  $-20.50 (\pm 0.65)$  to  $-22.45 (\pm 0.65) ^\circ\text{C}$ ,  
20 and the frozen fraction reaches unity at temperatures  $\leq -27.5 (\pm 0.5) ^\circ\text{C}$ . The  $f_{ice}$  of 47 mg/ml  
21 PWW droplets increase from 0 to 0.06 as the temperature is lowered from  $-4.50 (\pm 0.65)$  to  $-$   
22  $11.20 (\pm 0.65) ^\circ\text{C}$ , it then reaches unity at temperatures  $\leq -16.85 (\pm 0.55) ^\circ\text{C}$ . The results of  
23 Pummer et al. (2012) and Pummer et al. (2013), which are presented in Augustin et al. (2013),  
24 are also shown in Figure 7. These studies used a microscope equipped with a cryostage to  
25 investigate PWW emulsions of Silver birch (*Betula pendula*) (Pummer et al., 2012; Pummer  
26 2013; Augustin et al., 2013). The CEDB data using 5 mg/ml water birch (*Betula fontinalis*  
27 *occidentalis*) pollen PWW samples show a similar temperature dependent trend in  $f_{ice}$  to the  
28 50 mg/ml *Betula pendula* PWW droplets. Both the  $f_{ice}$  values for these two different species  
29 increase rapidly, from an initial value of  $\sim 0$  to 1, in the relatively small temperature range of  
30  $\sim 5 ^\circ\text{C}$ . The 0.1 mg/ml *Betula pendula* PWW droplets also have a similar shaped  $f_{ice}$  curve to  
31 the CEDB results but show subtle differences in freezing ability, compared to both the 5

1 mg/ml *Betula fontinalis occidentalis* sample and 50 mg/ml *Betula pendula* sample, with  $f_{ice}$   
2 only reaching a value of  $\sim 0.9$  before the onset of homogenous nucleation at  $\sim 37.5$  °C.

3 The similarity between the freezing curves of the two different pollen species from the same  
4 genus is intriguing; it suggests that the component(s) of PWW responsible for IN activity is  
5 common to the *Betula* genus. It should be noted that the pollen grains of both silver birch and  
6 water birch have very similar shapes with the characteristic raised pore structure of the *Betula*  
7 genus, but it seems unlikely that these macro features of the pollen structure will have  
8 significant influence on the freezing ability on the filtered birch PWW. It has been shown  
9 that saccharides, lipids and proteins are easily removed from pollen particles via aqueous  
10 extraction (Pummer et al. 2013). It has been suggested that the IN ability of birch pollen  
11 PWW is not due to proteinaceous compounds but rather sugar-like macromolecules with  
12 masses between 100 and 300 kDa (Pummer et al. 2012).

13 The differences between the  $f_{ice}$  values of different species are likely due to the different  
14 concentrations of the extractable compounds. These differences can even occur across  
15 samples from the same genus and species but from different geographical regions (Augustin  
16 et al., 2013). We speculate that the yellow colour of the water birch PWW solution maybe  
17 indicates that it contains a high concentration of carotenoids, which may be one of the  
18 compounds that could influence the immersion freezing of PWW. It is possible that  
19 differences between the CEDB and cryostage measurement techniques may also influence the  
20 observed differences: the CEDB measurement used monodisperse ( $\sim 30$   $\mu\text{m}$  diameter) sized  
21 PWW droplets, as opposed to the polydisperse PWW droplet size distribution (10 – 200  $\mu\text{m}$   
22 diameter) of the cryostage experiments by Pummer et al. (2012, 2013). It is noted that for a  
23 fixed concentration of PWW the sample volume is important for the freezing of PWW  
24 droplets and consequently the reported freezing fraction. In other words, the absolute number  
25 of IN active compounds in larger volume sample will be higher under the same concentration.  
26 Secondly the PWW droplets in the CEDB are charged and cooled over a different timescale  
27 compared to the cryostage experiments. Finally the contact free nature of the CEDB may  
28 influence the outcome.

29 In the real atmosphere bioaerosols will encounter a range of different RHs, within and out of  
30 clouds, and PWW will likely go through hydration and dehydration events. In order to  
31 investigate the effect of dehydration on IN ability of PWW, the 5 mg mL<sup>-1</sup> birch PWW was  
32 dehydrated within an oven set at a temperature of 80 °C. Subsequent to this drying step, it

1 was re-dissolved using HPLC grade deionized water. The mass fraction of the PWW before  
2 and after dehydration and subsequent rehydration was kept the same at 0.14%. The freezing  
3 fraction of re-dissolved 5 mg mL<sup>-1</sup> birch PWW is shown in Figure 8 (blue triangles) and  
4 compared to the original 5 mg mL<sup>-1</sup> PWW that was not subjected to the dehydration step (red  
5 circles). The two  $f_{ice}$  curves are found to be similar, firstly, the boundary temperature between  
6 observed ice nucleation and no ice nucleation PWW not subject to the dehydration step is at -  
7 20.5 ( $\pm 0.7$ ) °C, and for the re-dissolved PWW is at -16.7 ( $\pm 0.5$ ) °C. Secondly, both the  $f_{ice}$  of  
8 the original and re-dissolved 5 mg mL<sup>-1</sup> birch PWW exceed 0.8 while lowering the  
9 temperature by another 7 °C relative to the boundary temperature. The similarity in  
10 observations strongly indicates that dehydration of the sample does not significantly weaken  
11 the IN activity of PWW. Such a finding is in agreement with the conclusion by Pummer et al.  
12 (2012; 2013) and indicates that under various RH environments, the PWW residues will be  
13 efficient IN. Hence PWW residue will still be able to influence local precipitation by acting as  
14 highly active IN regardless of the RH history they encountered prior to the freezing event.

15

16 Pummer et al. (2012; 2013) analysed the IN activity of PWW after protein decomposition and  
17 suggested that the polysaccharide content of the PWW might be responsible for controlling  
18 the IN activity of PWW. With the purpose to analyse the IN activity of polysaccharides in a  
19 more direct way, we used a method similar to Galanos et al. (1969). Water saturated phenol  
20 (Tris-HCl saturated, pH 6.6/7.9, Amresco-Interchim, Biotechnology Grade) was used to  
21 remove proteins from PWW (Galanos et al. 1969). Briefly the protocol is as follows, initially  
22 5 mg mL<sup>-1</sup> birch PWW was generated using the procedure as described above. It was then  
23 mixed with water saturated phenol (1:1 v/v) and stirred by a mixer (Fisher Scientific Top Mix  
24 FB 15024) for 5 minutes. The mixture is then kept in the fridge overnight to allow the phenol  
25 phase to separate from the aqueous phase. The aqueous phase will now be deficient of the  
26 protein fraction which preferentially partitions to the less polar phenol phase. We henceforth  
27 refer to this aqueous phase as the 'phenol extracted PWW'. The mass fraction of the 'phenol  
28 extracted PWW' is obtained by performing a dehydration and rehydration once the mass of  
29 the residue is known.

30

31 The freezing fraction of 'phenol extracted PWW' is shown in Figure 8 (pink triangle) and  
32 compared to the non-extracted PWW. It can be seen that the removal of the proteinaceous



1 component leads to a less effective IN. Interestingly the  $f_{ice}$  curve of the ‘phenol extracted  
2 PWW’ can be separated into two distinct stages according to the slope. In the first stage, the  
3 value of  $f_{ice}$  increases from 0 to 0.11 as null point temperature lowering from  $-20.8 (\pm 0.5) ^\circ\text{C}$   
4 to  $23.3 (\pm 0.8) ^\circ\text{C}$ , afterwards a plateau appears as the temperature continually going down to -  
5  $26.7 (\pm 0.8) ^\circ\text{C}$  with  $f_{ice} = 0.13$ . In the second stage, the freezing fraction jumps steeply to 0.76  
6 at  $-27.7 (\pm 0.8) ^\circ\text{C}$  and finally up to 1 at  $-27.7 (\pm 0.8) ^\circ\text{C}$  when the temperature arrives to  $-29.6$   
7  $(\pm 0.9) ^\circ\text{C}$ . Such distinct stages within the  $f_{ice}$  curve is indicative of different IN species within  
8 the PWW. Hence we infer that at least two kind of IN active compounds have been left in the  
9 water phase after dealing with phenol. These were not observed in the PWW samples  
10 because of the greater IN ability of the proteinaceous fraction.

11 Additionally, we also observed the IN behaviour of lower concentration ( $mf=0.09\%$ ) ‘phenol  
12 extracted PWW’ and shown it in Figure 8 (Olive triangle). The significant increasing of  $f_{ice}$   
13 start from  $-26.4 ^\circ\text{C}$  with a value of 0.13 and increased to 0.76 at  $-29.8 ^\circ\text{C}$ . As expected, this  
14 curve indicates that lower concentrations of the polysaccharide rich material result in a lower  
15 IN activity of PWW droplet.

16 The experimental results presented in this study, in combination with other literature  
17 (Pummer et al., 2012; Augustin et al., 2013), indicate that birch PWW droplets are active in  
18 the immersion mode of freezing at relatively warm temperatures. Extraction of the  
19 proteinaceous component of the PWW indicates that the proteins are likely the most IN active  
20 component of PWW. However the non-proteinaceous component (likely polysaccharides) is  
21 still IN active albeit at a lower temperature. However the freezing temperatures are lower  
22 than that observed for birch (*Betula alba*) pollen grains in the contact, immersion and  
23 condensation modes of freezing (Diehl et al., 2001; Diehl et al., 2002). The IN activity  
24 behaviour shown by the birch PWW suggests significant potential for cloud formation and  
25 precipitation especially due to the wide geographical extent of birch.

26

## 27 **4 Conclusions**

28 This paper introduces a new design of CEDB. Furthermore it reports the initial applications  
29 of this CEDB to measure the evaporation kinetics and freezing properties of SWD. Accurate  
30 size and phase determination of the single levitated SWD was characterized via measurement  
31 of the Mie scattering signal. The rate of evaporation of SWD in a dry gaseous environment  
32 was determined, in the temperature range from  $-5 - -34.5 ^\circ\text{C}$  and the current setup allows the

1 freezing experiments to be performed within a time window of up to one minute dependent on  
2 temperature. The phase transition of the PWW particle from liquid to frozen solid, and hence  
3 the freezing efficiency of PWW, was characterized through the loss of the regular Mie  
4 scattering signal from the levitated droplet. From this data, the statistical freezing fractions of  
5 PWW droplets were obtained in the temperature range: -4.5 – -40 °C. It was found that that  
6 PWW from water birch (*Betula fontinalis occidentalis*) pollen, in common with other *Betula*  
7 species (Pummer et al., 2012; Augustin et al., 2013) is IN active in the immersion freezing  
8 mode at relatively warm temperatures: -22 °C and below. The evaporation and freezing  
9 results from this study illustrate the versatility of the new CEDB system for studying subzero  
10 phenomena in a contact free technique. The CEDB instrument will be used in future  
11 experiments to study a range of freezing phenomena and their implications for atmospheric  
12 ice nucleation.

13

#### 14 **Acknowledgements**

15 This study was supported by NERC via the ACID-PRUF consortium grant (NE/I020105/1).  
16 We thank Jonathan Reid and James Davis for providing detailed information about their EDB  
17 design. We thank Thomas Leisner for good advice and providing the opportunity to visit his  
18 EDB laboratory. We thank Hinrich Grothe and Bernhard Pummer for provision of their PWW  
19 data sets.

20

21

## 1 **References**

- 2 Atkinson, J. D., Murray, B.J., Woodhouse, M. T., Whale, T. F., Baustian, K. J., Carslaw, K.  
3 S., Dobbie, S., O'Sullivan, D., and Malkin, T. L.: The importance of feldspar for ice  
4 nucleation by mineral dust in mixed-phase clouds. *Nature*, 498, 355-358, 2013.
- 5 Augustin, S., Wex, H., Niedermeier, D., Pummer, B., Grothe, H., Hartmann, S., Tomsche, L.,  
6 Clauss, T., Voigtländer, J., Ignatius, K., and Stratmann, F.: Immersion freezing of birch pollen  
7 washing water, *Atmos. Chem. Phys.*, 13, 10989-11003, 2013.
- 8 Aylor, D. E.: Settling speed of corn (*Zea mays*) pollen. *J. Aerosol Sci.* 33, 1601-1607, 2002.
- 9 Cantrell, W., and Heymsfield, A.: Production of Ice in Tropospheric Clouds: A Review. *Bull.*  
10 *Amer. Meteor. Soc.*, 86, 795-807, 2005.
- 11 Choi, M. Y., and Chan, C. K.: The Effects of Organic Species on the Hygroscopic Behaviors  
12 of Inorganic Aerosols. *Environ. Sci. Technol.*, 36, 2422-2428, 2002.
- 13 Crawford, I., Möhler, O., Schnaiter, M., Saathoff, H., Liu, D., McMeeking, G., Linke, C.,  
14 Flynn, M., Bower, K. N., Connolly, P. J. Gallagher, M. W., and Coe, H.: Laboratory studies  
15 of immersion and deposition mode ice nucleation of ozone aged mineral dust particles. *Atmos.*  
16 *Chem. Phys.* 11, 9549-9561, 2011.
- 17 Creamean, J. M., Suski, K. J., Rosenfeld, D., Cazorla, A., DeMott, P. J., Sullivan, R. C.,  
18 White, A. B., Ralph, F. M., Minnis, P., Comstock, J. M., Tomlinson, J. M., and Prather, K. A.:  
19 Dust and biological aerosols from the Sahara and Asia influence precipitation in the western  
20 US, *Science*, 339, 1572-1578, 2013.
- 21 Davis, E. J.: A history of single aerosol particle levitation. *Aerosol Sci. Technol.*, 26(3), 212-  
22 254, 1997.
- 23 Davies, J. F., Haddrell, A. E., and Reid, J. P.: Time-Resolved Measurements of the  
24 Evaporation of Volatile Components from Single Aerosol Droplets. *Aerosol Sci. Technol.*  
25 46(6), 666-677, 2012.
- 26 Davies, J. F., Miles, R. E. H., Haddrell, A. E., and Reid, J. P.: Influence of organic films on  
27 the evaporation and condensation of water in aerosol. *Proc. Nat. Acad. Sci. USA*, 110(22),  
28 8807-8812, 2013.
- 29 **Davies, J. F., Miles, R. E. H., Haddrell, A. E., and Reid, J. P.: Temperature dependence of the**

- 1 vapor pressure and evaporation coefficient of supercooled water. *J. Geophys. Res. Atmos.*,  
2 119, 10931-10940, 2014.
- 3 Deguillaume, D., Leriche, M., Amato, P., Ariya, P. A., Delort, A.-M., Pöschl, U.,  
4 Chaumerliac, N., Bauer, H., Flossmann, A. I., and Morris, C. E.: Microbiology and  
5 atmospheric processes: chemical interactions of primary biological aerosols. *Biogeosciences*,  
6 5, 1073-1084, 2008.
- 7 DeMott, P. J., Prenni, A. J., Liu, X., Kreidenweis, S. M., Petters, M. D., Twohy, C. H.,  
8 Richardson, M. S., Eidhammer, T., and Rogers, D. C.: Predicting global atmospheric ice  
9 nuclei distributions and their impacts on climate. *P. Natl. Acad. Sci. USA*, 107, 11217-11222,  
10 2010.
- 11 Després, V. R., Nowoisky, J. F., Klose, M., Conrad, R., Andreae, M. O., and Pöschl, U.:  
12 Characterization of primary biogenic aerosol particles in urban, rural, and high-alpine air by  
13 DNA sequence and restriction fragment analysis of ribosomal RNA genes. *Biogeosciences*, 4,  
14 1127-1141, 2007.
- 15 Després, L., David, J. P., and Gallet, C.: The evolutionary ecology of insect resistance to plant  
16 chemicals. *Trends in Ecology & Evolution*, 22, 298-307, 2007.
- 17 Diehl, K., Quick, C., Matthias-Maser, S., Mitra, S. K., and Jaenicke, R.: The ice nucleating  
18 ability of pollen. Part I: Laboratory studies in deposition and condensation freezing modes,  
19 *Atmos. Res.*, 58, 75-87, 2001.
- 20 Diehl, K., Matthias-Maser, S., Jaenicke, R., and Mitra, S. K.: The ice nucleating ability of  
21 pollen: Part II. Laboratory studies in immersion and contact freezing modes, *Atmos. Res.*, 61,  
22 125-133, 2002.
- 23 Galanos, C., Lüderitz, O., and Westphal, O.: A new method for the extraction of R  
24 Lipopolysaccharides. *European J. Biochem.* 1969, 9, 245-249.
- 25 Glantschnig, W. J.;and Chen, S.-H.: Light scattering from water droplets in the geometrical  
26 optics approximation. *Appl. Opt.* 20, 2499-2509, 1981.
- 27 Griffiths, P. T., Borlace, J.-S., Gallimore, P. J., Kalberer, M., Herzog, M., Pope, F. D.:  
28 Hygroscopic growth and cloud activation of pollen: a laboratory and modelling study. *Atmos.*  
29 *Sci. Let.* 13, 289-295, 2012.
- 30 Heinisch, C., Bakić, C., Damaschke, N., Petter, J., Tschudi, T., and Tropea, C.: Neue

1 Paulfallengeometrie Zur Fixierung Von Tropfen Und Partikeln In Gasströmungen Mit 360°-  
2 Zugang Für Laserdiagnostik. 14 Fachtagung Lasermethoden in der Strömungsmesstechnik,  
3 PTB, Braunschweig. 2.61-2.66, 2006.

4 Heinisch, C., Wills, J. B. Reid, J. P., Tschudi, T., and Tropea, C.: Temperature measurement  
5 of single evaporating water droplets in a nitrogen flow using spontaneous Raman scattering.  
6 *Phys. Chem. Chem. Phys.* 11(42), 9720-9728, 2009.

7 Heise, H. A., and Heise, E. R.: The distribution of ragweed pollen and alternaria spores in the  
8 upper atmosphere *J. Allergy*. **19** 403-407, 1948.

9 Helbig, N., Vogel, B., Vogel, H. and Fiedler, F.: Numerical modelling of pollen dispersion on  
10 the regional scale *Aerobiologia* 3, 3-19, 2004.

11 Hirschfelder, J. O., Curtiss, C. F., and Bird, R. B.: Molecular theory of gases and liquids. John  
12 Wiley & Sons, Inc., New York., 1954.

13 Hoffmann, N., Duft, D., Kiseleva, A., and Leisner, T.: Contact freezing efficiency of mineral  
14 dust aerosols studied in an electrodynamic balance: quantitative size and temperature  
15 dependence for illite particles. *Faraday Discuss.*, 165, 383-390, 2013.

16 Hoffmann, N., Kiselev, A., Rzesanke, D., Duft, D., and Leisner, T.: Experimental  
17 quantification of contact freezing in an electrodynamic balance. *Atmos. Meas. Tech.*, 6, 2373-  
18 2382, 2013.

19 Hogan, R. J., Behera, M. D., O'Connor, E. J., and Illingworth, A. J.: Estimate of the global  
20 distribution of stratiform supercooled liquid water clouds using the LITE lidar. *Geophys. Res.*  
21 *Lett.*, 31, L05106, doi: 10.1029/2003GL018977, 2004.

22 Holyst, R., Litniewski, M., Jakubczyk, D., Kolwas, K., Kolwas, M., Kowalski, K., Migacz, S.,  
23 Palesa, S., and Zientara, M.: Evaporation of freely suspended single droplets: experimental,  
24 theoretical and computational simulations. *Rep. Prog. Phys.* 76, 034601 (19pp), 2013.

25 Hoose, C., Kristjánsson, J. E., Burrows, S. M.: How important is biological ice nucleation in  
26 clouds on a global scale? *Environ. Res. Lett.* 5, 024009 (7pp), 2010.

27 Hoose, C., and Möhler, O.: Heterogeneous ice nucleation on atmospheric aerosols: a review of  
28 results from laboratory experiments. *Atmos. Chem. Phys.*, 12, 9817-9854, 2012.

29 Kanji, Z. A., Welti, A., Chou, C., Stetzer, O., and Lohmann, U.: Laboratory studies of  
30 immersion and deposition mode ice nucleation of ozone aged mineral dust particles. *Atmos.*

1 Chem. Phys. 13, 9097-9118, 2013.

2 Knopf, D. A., Alpert, P. A., Wang, B., and Aller, J. Y.: Stimulation of ice nucleation by  
3 marine diatoms. *Nat. Geosci.* 4, 88-90, 2011.

4 Koop, T., Luo, B., Tsias, A., and Peter T.: Water activity as the determinant for homogeneous  
5 ice nucleation in aqueous solutions. *Nature*, 406, 611-614, 2000.

6 Krämer, B., Hübner, O., Vortisch, H., Wöste, L., and Leisner, T., Schwell, M., Rühl, E., and  
7 Baumgärtel, H.: Homogeneous nucleation rates of supercooled water measured in single  
8 levitated microdroplets. *J. Chem. Phys.* 111, 6521-6527, 1999.

9 Krieger, U. K., Colberg, C. A., Weers, U., Koop, T., and Peter, T.: Supercooling of single  
10 H<sub>2</sub>SO<sub>4</sub>/H<sub>2</sub>O aerosols to 158 K: No evidence for the occurrence of the octahydrate.  
11 *Geophysical Research Letters*, 27, 2097-2100, 2000.

12 Krieger, U. K., Marcolli, C., and Reid, J. P.: Exploring the complexity of aerosol particle  
13 properties and processes using single particle techniques. *Chem. Soc. Rev.*, 41, 6631-6662,  
14 2012.

15 Kulmala, M., Vesala, T., Wagner, P. E.: An analytical expression for the rate of binary  
16 condensational particle growth. *Proc. R. Soc. London, Ser. A-Math. Phys. Eng. Sci.* 1993, 441,  
17 589-605.

18 Laaksonen, A., Talanquer, V., and Oxtoby, D. W.: NUCLEATION: Measurements, Theory,  
19 and Atmospheric Applications. *Annu. Rev. Phys. Chem.*, 46, 489-524, 1995.

20 Ladino Moreno, L. A., Stetzer, O., and Lohmann, U.: Contact freezing: a review of  
21 experimental studies. *Atmos. Chem. Phys.*, 13, 9745-9769, 2013.

22 Lee, A. K. Y. and Chan C. K.: Single particle Raman spectroscopy for investigating  
23 atmospheric heterogeneous reactions of organic aerosols. *Atmos. Environ*, 41, 4611-4621,  
24 2007.

25 Lee, A. K. Y., Ling, T. Y. and Chan, C. K.: Understanding hygroscopic growth and phase  
26 transformation of aerosols using single particle Raman spectroscopy in an electrodynamic  
27 balance. *Faraday Discuss.* 137, 245-263, 2008.

28 Lee, J. W. L., Carrascón, V., Gallimore, P. J., Fuller, S. J., Björkegren, A., Spring, D. A.,  
29 Pope, F. D., and Kalberer, K.: The effect of humidity on the ozonolysis of unsaturated  
30 compounds in aerosol particles. *Phys. Chem. Chem. Phys.* 14(22), 8023-8031, 2012.

- 1 Li K.-Y., Tu, H., Ray, A. K.: Charge Limits on Droplets during Evaporation. *Langmuir* 21,  
2 3786-3794, 2005.
- 3 Lohmann, U., and Feichter, J.: Global indirect aerosol effects: a review. *Atmos. Chem. Phys.*,  
4 5, 715-737, 2005.
- 5 Mie, G.: Beiträge zur Optik Trüber Medien, Speziell Kolloidaler Metallösungen. *Ann. Phys.*  
6 25, 377-445, 1908.
- 7 Miles, R. E. H., Reid, J. P., Riipinen, I.: Comparison of Approaches for Measuring the Mass  
8 Accommodation Coefficient for the Condensation of Water and Sensitivities to Uncertainties  
9 in Thermophysical Properties. *J. Phys. Chem. A* 116, 10810-10825, 2012.
- 10 Möhler, O., DeMott, P. J., Vali, G., and Levin, Z.: Microbiology and atmospheric processes:  
11 the role of biological particles in cloud physics. *Biogeosciences*, 4, 1059-1071, 2007.
- 12 Moller, B., Rarey, J., and Ramjugernath, D.: Estimation of the vapour pressure of non-  
13 electrolyte organic compounds via group contributions and group interactions. *J. Mol. Liq.*  
14 143, 52-63, 2008.
- 15 Murphy, B. D., and Koop, T.: Review of the vapour pressures of ice and supercooled water  
16 for atmospheric applications. *Q. J. R. Meteorol. Soc.* 131, 1539-1565, 2005.
- 17 Murray, B. J., Wilson, T. W., Dobbie, S., Cui, Z., Al-Jumur, S. M. R. K., Möhler, O.,  
18 Schnaiter, M., Wagner, R., Benz, S., Niemand, M., Saathoff, H., Ebert, V., Wagner, S., and  
19 Kärcher.: Heterogeneous nucleation of ice particles on glassy aerosols under cirrus conditions.  
20 *Nat. Geosci.* 3, 233-237, 2010.
- 21 Murray, B. J., O'Sullivan, D., Atkinson, J. D., and Webb, M. E.: Ice nucleation by particles  
22 immersed in supercooled cloud droplets. *Chem. Soc. Rev.*, 41, 6519-6554, 2012.
- 23 Niedermeier, D., Hartmann, S., Shaw, R. A., Covert, D., Mentel, T. F., Schneider, J., Poulain,  
24 L., Reitz, P., Spindler, C., Clauss, T., Kiselev, A., Hallbauer, E., Wex, H., Mildenerger, K.,  
25 and Stratmann, F.: Heterogeneous freezing of droplets with immersed mineral dust particles –  
26 measurements and parameterization, *Atmos. Chem. Phys.*, 10, 3601-3614, 2010.
- 27 Parsons, M. T., Riffell, J. L., and Bertram, A. K.: Crystallization of aqueous inorganic-  
28 malonic acid particles: Nucleation rates, dependence on size, and dependence on the  
29 ammonium-to-sulfate, *J. Phys. Chem. A*, 110, 8108-8115, 2006.
- 30 Pope, F. D.: Pollen grains are efficient cloud condensation nuclei. *Environ. Res. Lett.* 5,

1 044015 (6pp), 2010.

2 Pope, F. D., Dennis-Smith, B. J., Griffiths, P. T., Clegg, S. L., Cox, R. A.: Studies of Single  
3 Aerosol Particles Containing Malonic Acid, Glutaric Acid, and Their Mixtures with Sodium  
4 Chloride. I. Hygroscopic Growth. *J. Phys. Chem. A* 114, 5335-5341, 2010.

5 Pope, F. D., Tong H.-J., Dennis-Smith, B. J., Griffiths, P. T., Clegg, S. L., Reid, J. P., Cox,  
6 R. A.: Studies of Single Aerosol Particles Containing Malonic Acid, Glutaric Acid, and Their  
7 Mixtures with Sodium Chloride. II. Liquid-State Vapor Pressures of the Acids. *J. Phys. Chem.*  
8 *A* 114, 10156-10165, 2010.

9 Pope, F. D., Gallimore, P. J., Fuller, S. J., Cox, R. A., and Kalberer, M.: Ozonolysis of maleic  
10 acid aerosols: Initial results on aerosol hygroscopicity and volatility. *Environ. Sci. Technol.*  
11 44, 6656-6660, 2010.

12 Pöschl, U.: Atmospheric Aerosol: Composition, Transformation, Climate and Health Effects.  
13 *Angew. Chem. Int. Ed.*, 44, 7520-7540, 2005.

14 Pratt, K. A., DeMott, P. J., French, J. R., Wang, Z., Westphal, D. L., Heymsfield, A. J.,  
15 Twohy, C. H., Prenni, A. J., and Prather, K. A.: In situ detection of biological particles in  
16 cloud ice-crystals. *Nat. Geosci.* 2, 398-401, 2009.

17 Prenni, A. J., Petters, M. D., Kreidenweis, S. M., Heald, C. L., Martin, S. T., Artaxo, P.,  
18 Garland, R. M., Wollny, A. G., and Pöschl U.: Relative roles of biogenic emissions and  
19 Saharan dust as ice nuclei in the Amazon basin. *Nat. Geosci.*, 2, 401-404, 2009.

20 Pruppacher, H. R., and Klett, J. D.: *Microphysics of Clouds and Precipitation*, Atmospheric  
21 and Oceanographic Sciences Library, Kluwer Academic Press, Dordrecht, The Netherlands,  
22 1997.

23 Pummer, B. G., Bauer, H., Bernardi, J., Bleicher, S., and Grothe, H.: Suspendable  
24 macromolecules are responsible for ice nucleation activity of birch and conifer pollen, *Atmos.*  
25 *Chem. Phys.*, 12, 2541-2550, 2012.

26 Pummer, B. G.: Ice nucleation activity of pollen and fungal spores, PhD Dissertation,  
27 Technische Universität Wien, 2013.

28 Pummer, B. G., Bauer, H., Bernardi, J., Chazallon, B., Facq, S., Lendl, B., Whitmore, K., and  
29 Grothe, H.: Chemistry and morphology of dried-up pollen suspension residues. *J. Raman*  
30 *Spectrosc.* 44, 1654-1658, 2013.



1 Rauber, R. M., and Tokay, A.: An Explanation for the Existence of Supercooled Water at the  
2 Top of Cold Clouds. *J. Atmos. Sci.*, 48, 1005-1023, 1991.

3 Rosenfeld, D., and Woodley, W. L.: Deep convective clouds with sustained supercooled  
4 liquid water down to -37.5 °C. *Nature*, 405, 440-442, 2000.

5 Rousseau, D-D., Duzer, D., Cambon, G, Jolly, D., Poulsen, U., Ferrier, J., Schevin, P., and  
6 Gros, R.: Long distance transport of pollen to Greenland *Geophys. Res. Lett.* 30, 1765,  
7 doi:10.1029/2003GL017539, 2003.

8 Sassen, K.: Highly supercooled cirrus cloud water: confirmation and climatic implications.  
9 *Science*, 227, 411-413, 1985.

10 Schäppi, G. F., Taylor, P. E., Pain, M. C. F., Cameron, P. A., Dent, A. W., Staff, I. A., and  
11 Suphioglu, C.: Concentrations of major grass group 4 allergens in pollen grains and  
12 atmospheric particles: implications for hay fever and allergic asthma sufferers sensitized to  
13 grass pollen allergens. *Clin. Exp. Allergy*, 29, 633-641, 1999.

14 Seinfeld, J. H., Pandis, S. N.: *Atmospheric Chemistry and Physics: From Air Pollution to*  
15 *Climate Change*. New York: Wiley, 1998.

16 Shaw, R. A., Lamb, D., and Moyle, A.M.: An Electrodynamic Levitation System for Studying  
17 Individual Cloud Particles under Upper-Tropospheric Conditions. *J. Atmos. Ocean. Technol.*  
18 17, 940-948, 2000.

19 Sofiev, M., Siljamo, P., Ranta, H., and Rantio-Lehtimäki, A.: Towards numerical forecasting  
20 of long-range air transport of birch pollen: theoretical considerations and a feasibility study  
21 *Int. J. Biometeorol.* 50 392-402, 2006.

22 Soonsin, V., Zardini, A. A., Marcolli, C., Zuend, A., and Krieger, U. K.: The vapor pressures  
23 and activities of dicarboxylic acids reconsidered: the impact of the physical state of the  
24 aerosol. *Atmos. Chem. Phys.*, 10, 11753-11767, 2010.

25 Stöckel, P., Weidinger, I. M., Baumgärtel, H., and Leisner, T.: Rates of Homogeneous Ice  
26 Nucleation in Levitated H<sub>2</sub>O and D<sub>2</sub>O Droplets. *J. Phys. Chem. A* 109, 2540-2546, 2005.

27 Stratmann, F., Kiselev, A., Wurzler, S., Wendisch, M., Heintzenberg, J., Charlson, R. J.,  
28 Diehl, K., Wex, H., and Schmidt, S.: Laboratory studies and numerical simulations of cloud  
29 droplet formation under realistic supersaturation conditions, *J. Atmos. Ocean. Tech.*, 21, 876–  
30 887, 2004.

1 Svensson, E. A., Delval, C., Hessberg, P. von., Johnson, M. S., and Pettersson, J. B. C.:  
2 Freezing of water droplets colliding with kaolinite particles. *Atmos. Chem. Phys.*, 9, 4295-  
3 4300, 2009.

4 Swanson, B. D., Bacon, N. J., Davis, E. J., and Baker, M. B.: Electrodynamic trapping and  
5 manipulation of ice crystals. *Q. J. R. Meteorol. Soc.* 125, 1039-1058, 1999.

6 Tang, I. N., and Munkelwitz, H. R.: Water activities, densities, and refractive indices of  
7 aqueous sulfates and sodium nitrate droplets of atmospheric importance, *J. Geophys. Res.*, 99,  
8 18801-18808, 1994.

9 Tong, H.-J., Reid, J. P., Bones, D. L., Luo B. P., and Krieger, U.K.: Measurements of the  
10 timescale  $\tau$  for the mass transfer of water in glassy aerosol at low relative humidity and  
11 ambient temperature. *Atmos. Chem. Phys.*, 11, 4739-4754, 2011.

12 Haynes, W. M.: *CRC Handbook of Chemistry and Physics*, 94<sup>th</sup> Edition. CRC Press, Taylor  
13 & Francis Group, P. 6-164, 2013.

14 Vortisch, H. Krämer, B., Weidinger, I., Wöste, L., Leisner, T., Schwell, M. Baumgärtel, H.,  
15 and Rühl, E.: Homogeneous freezing nucleation rates and crystallization dynamics of single  
16 levitated sulfuric acid solution droplets. *Phys. Chem. Chem. Phys.* 2, 1407-1413, 2000.

17 Yttri, K. E., Dye, C., and Kiss, G.: Ambient aerosol concentrations of sugars and sugar-  
18 alcohols at four different sites in Norway, *Atmos. Chm. Phys.*, 7, 4267-4279, 2007.

19 Zhang, Y. H. and Chan, C. K.: Study of Contact Ion Pairs of Supersaturated Magnesium  
20 Sulfate Solutions using Raman Scattering of Levitated Single Droplets., *J. Phys. Chem A.*,  
21 104, 9191-9196, 2000.

22 Zobrist, B., Soonsin, V., Luo, B P., Krieger, U. K. Marcolli, C., Peter, T., and Koop, T.:  
23 Ultra-slow water diffusion in aqueous sucrose glasses. *Phys. Chem. Chem. Phys.*, 13, 3514-  
24 3526, 2011.

25

1

2

Table 1. Temperature gradients around the null point of the CEDB

3

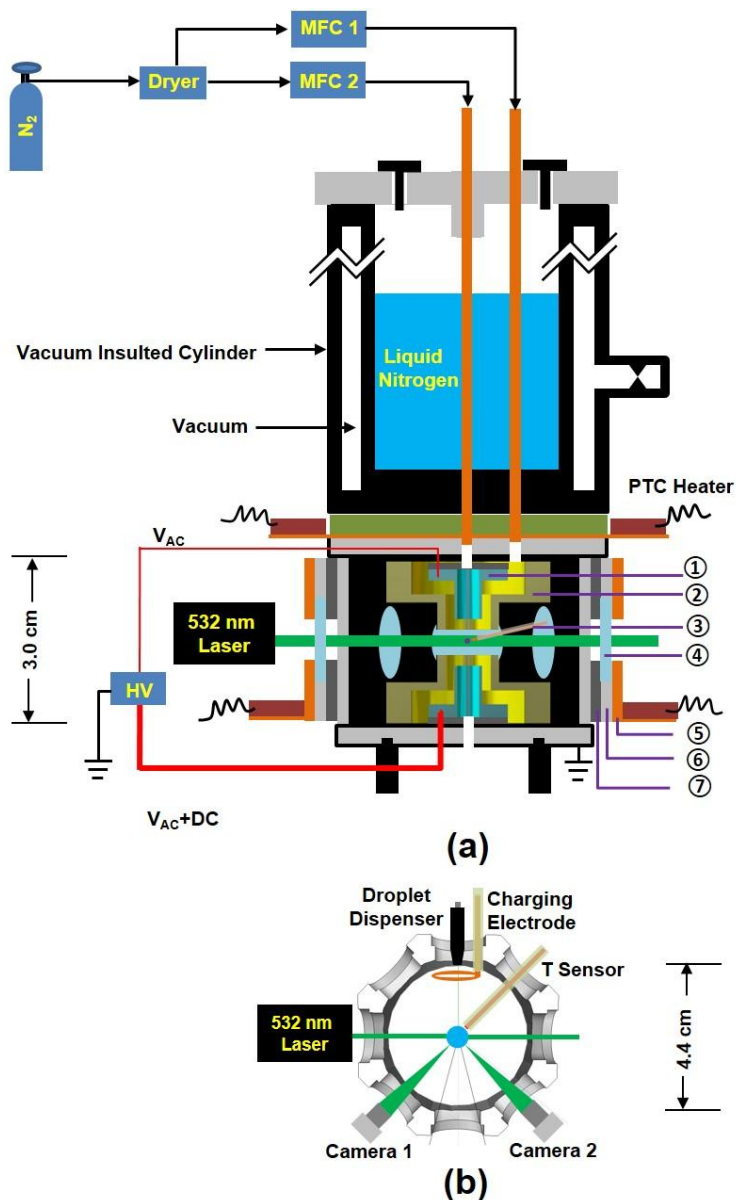
T <sub>-centre</sub> /°C	T1/°C	T2/°C	T3/°C
-41.9	-46.2	-36.2	-39.8
-36.5	-39	-31.8	-34.2
-25.7	-28.7	-22.2	-23.9
-13.1	-15	-7.2	-11.4
-5.2	-8.2	-0.55	-4

4 T1: Temperature 2mm above the centre, T2: Temperature 2mm below the centre T3:

5 Temperature 2mm radially away from the centre,

6

1 **Figures:**



2

3

4 Figure 1. (a) Schematic diagram of the new CEDB system. ① Inner electrode. ② Outer electrode. ③

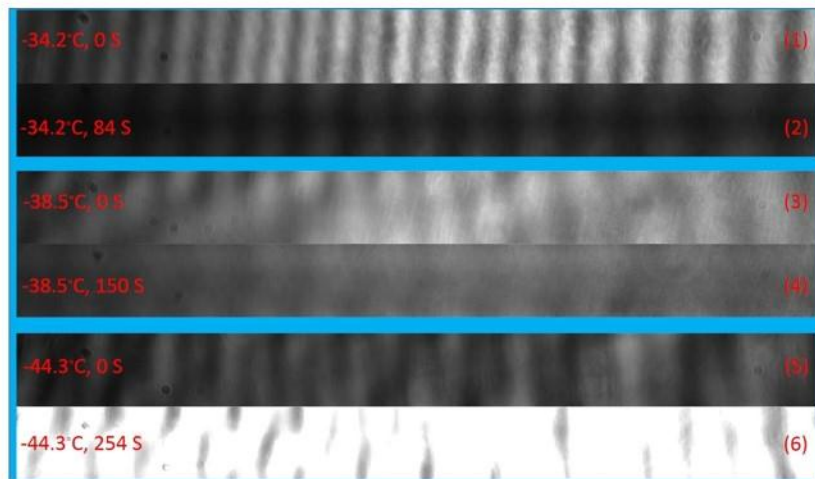
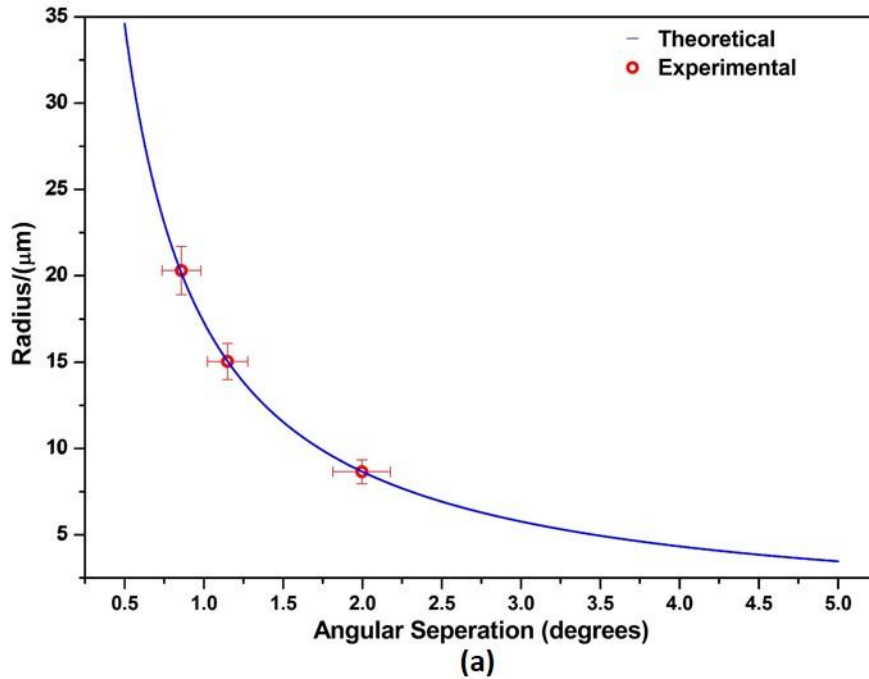
5 Thermocouple or relative humidity sensor. ④ Glass window. ⑤ Heating jacket. ⑥ Holder for glass

6 window. ⑦ Rubber insulator. (b) The top view of the schematic diagram of optical design,

7 dispensing and charging devices, and the thermocouple within the CEDB system. Cameras 1 and 2

8 are for droplet positioning and Mie scattering observation respectively.

9



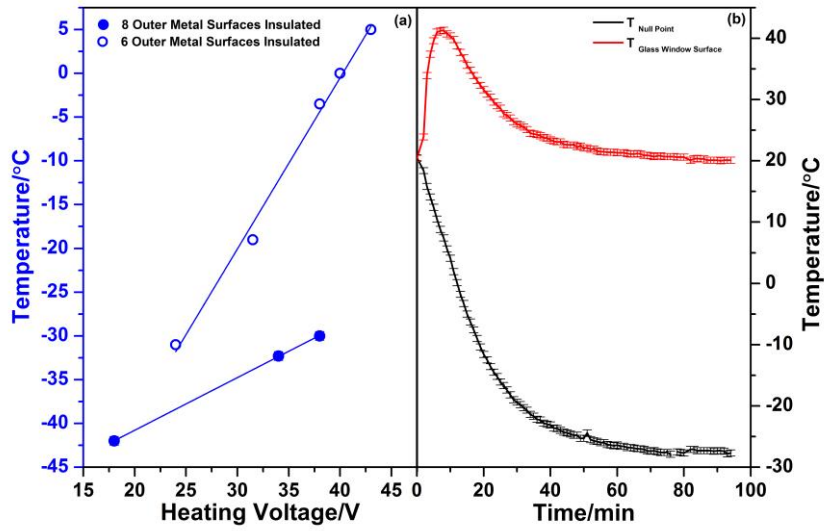
(b)

1

2 Figure 2. (a) Measurement of particle radius by elastic Mie scattering. The size calibration is achieved  
 3 using calibrated lime soda spheres. Blue line represents the calculated size based on the peak-to-peak  
 4 spacing using Equation (1). The experimental points (red circles) are the measured peak-to-peak  
 5 separations in the recorded diffraction patterns against the quoted size. The uncertainty in the angular  
 6 separation is the standard deviation ( $1\sigma$ ) in the measurement and the uncertainty in size is the standard  
 7 deviation in particle size stated by the manufacturer. (b) Mie scattering of pure SWDs at three  
 8 different temperatures:  $-34\text{ }^{\circ}\text{C}$  ((1) and (2)),  $-38.5\text{ }^{\circ}\text{C}$  ((3) and (4)),  $-44.3\text{ }^{\circ}\text{C}$  ((5) and (6)). Droplets at  $-$   
 9  $38.5$  and  $-44.3\text{ }^{\circ}\text{C}$  are homogeneously nucleated with irregular scattering patterns.

10

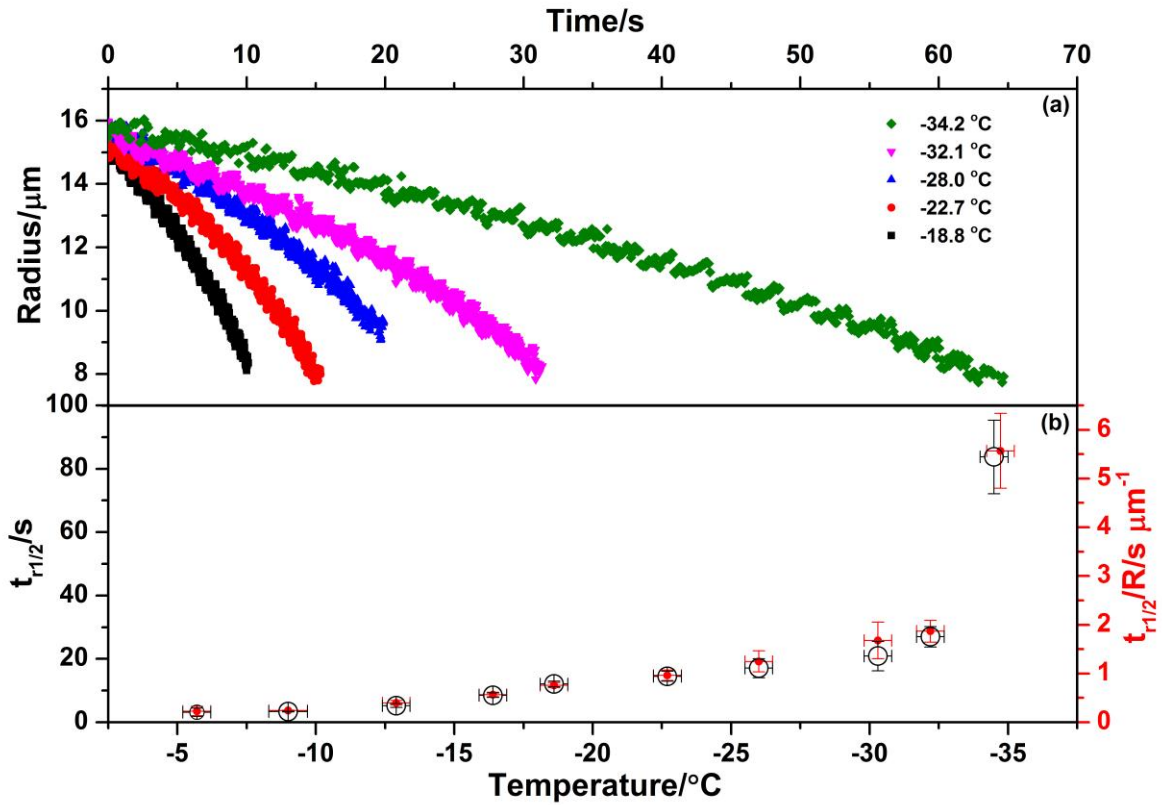
1



2

3 Figure 3. Temperature characterisation curves for the null point region of the CEDB. Two different  
4 insulation schemes allow to access different temperature ranges in the EDB. (a) Final temperature  
5 reached when 8 outer metal surfaces (blue solid circles) or 6 outer metal surfaces are insulated (blue  
6 circles) CEDB chamber versus heating voltage. (b) An example of glass window surface (red line) and  
7 null point (black line) temperature to reach  $-28^{\circ}\text{C}$  with 24 V heating voltage.

8



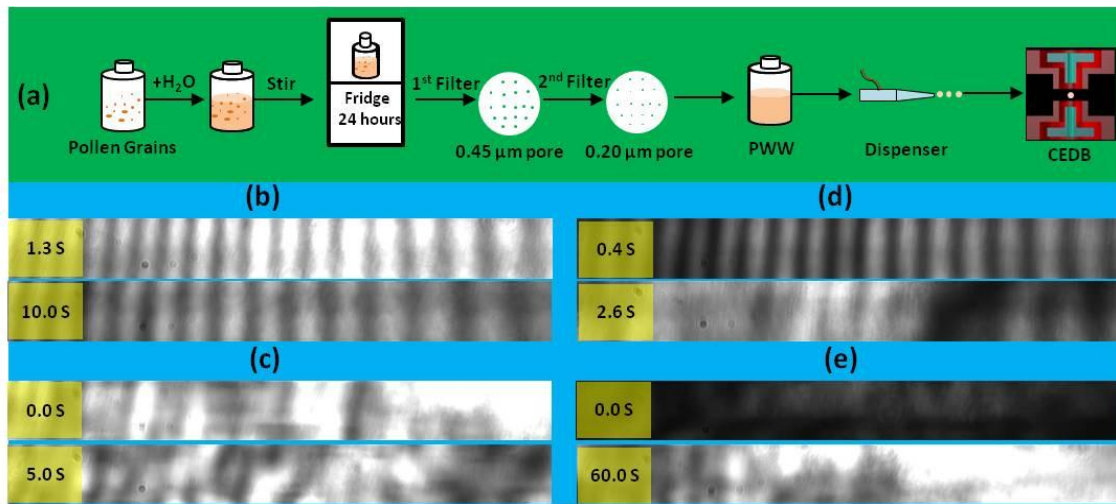
1

2 Figure 4. (a) Example evaporation decay traces of SWD at five different sub-zero temperatures. (b)  
 3  $t_{r/2}$  of SWDs at 10 different temperatures (black circles), and the ratio of  $t_{r/2}$  to radius ( $t_{r/2}/R$ )  
 4 estimated for the change of SWD for a series of temperature measurements (red dots). The  
 5 temperature error is the value stated by the manufacturer. The y-error for the  $t_{r/2}$  and  $t_{r/2}/R$  is the  
 6 standard deviation of the measurement. At least three individual experiments at each temperature  
 7 were conducted.

8

9

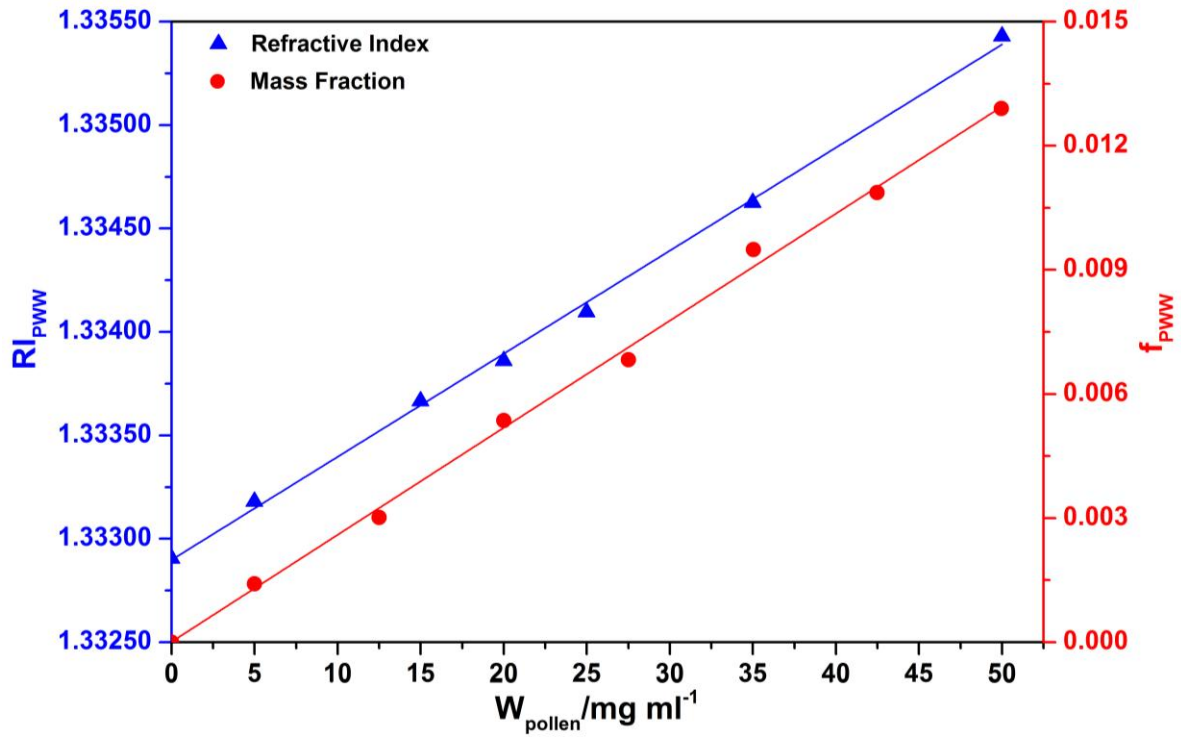
10



1  
2  
3  
4  
5  
6  
7  
8  
9  
10  
11  
12  
13  
14  
15  
16  
17  
18  
19  
20

Figure 5. Extraction procedure and example phase dependent elastic Mie scattering images. (a) Cartoon of extraction procedure of PWW solutions. (b) The phase function of an evaporating PWW particle at -21.8 °C and recorded at 1.3 (top) and 10.0 s (bottom). (c) The irregular phase functions of a PWW particle that froze immediately after injection at -24.2°C. (d) The recorded phase functions of a PWW particle that froze after a very short delay at -24.2 °C. (e) The irregular phase functions of a PWW particle that froze immediately after injection at -32.2°C.





1

2 Figure 6. The mass fraction ( $f_{\text{PWW}}$ , red circles) and refractive index ( $RI_{\text{PWW}}$ , blue triangles) of PWW  
 3 solutions versus the pollen suspension concentration ( $W_{\text{pollen}}$ ). The red and blue lines are linear fits to  
 4 the data with adjusted- $R^2$  values of 0.9969 and 0.9981, respectively.

5

6

7

8

9

10

11

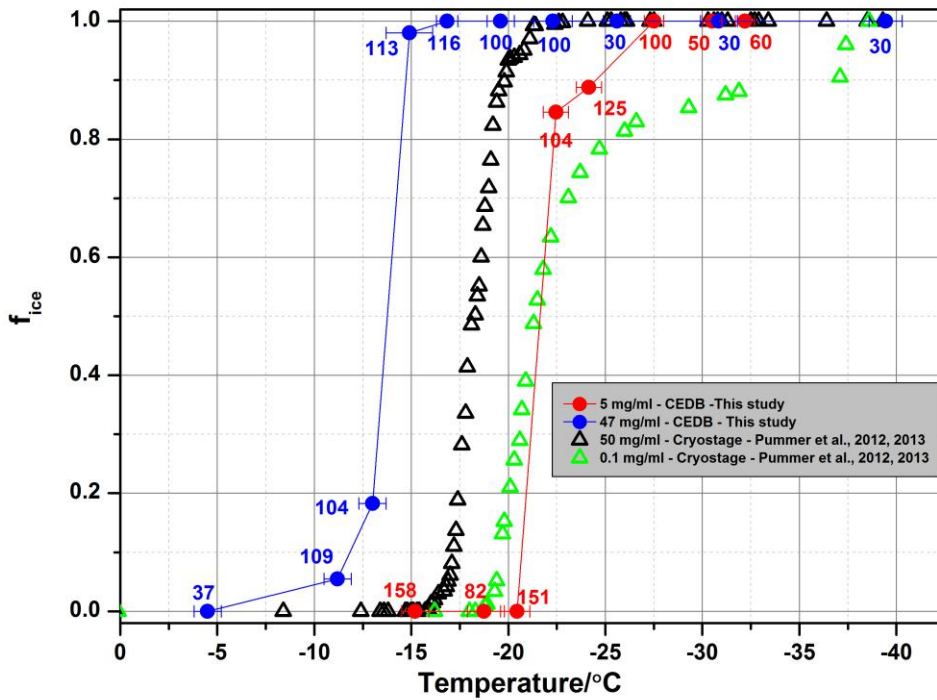
12

13

14

15

16



1

2 Figure 7. The temperature dependent freezing fraction ( $f_{ice}$ ) of 5 (red point and line) and 47 (blue  
 3 point and line) mg/ml birch PWW droplets. Data from this study (*Betula fontinalis occidentalis*,  
 4 CEDB) is compared to the data reported in Augustin et al. (2013) for *Betula pendula* obtained using  
 5 a cryostage microscope. The temperature error bar is calculated using both the stated probe accuracy  
 6 from the manufacturer plus the fluctuation of experimental temperature for each data point. The  
 7 number in the figure is the droplet number for each data point.

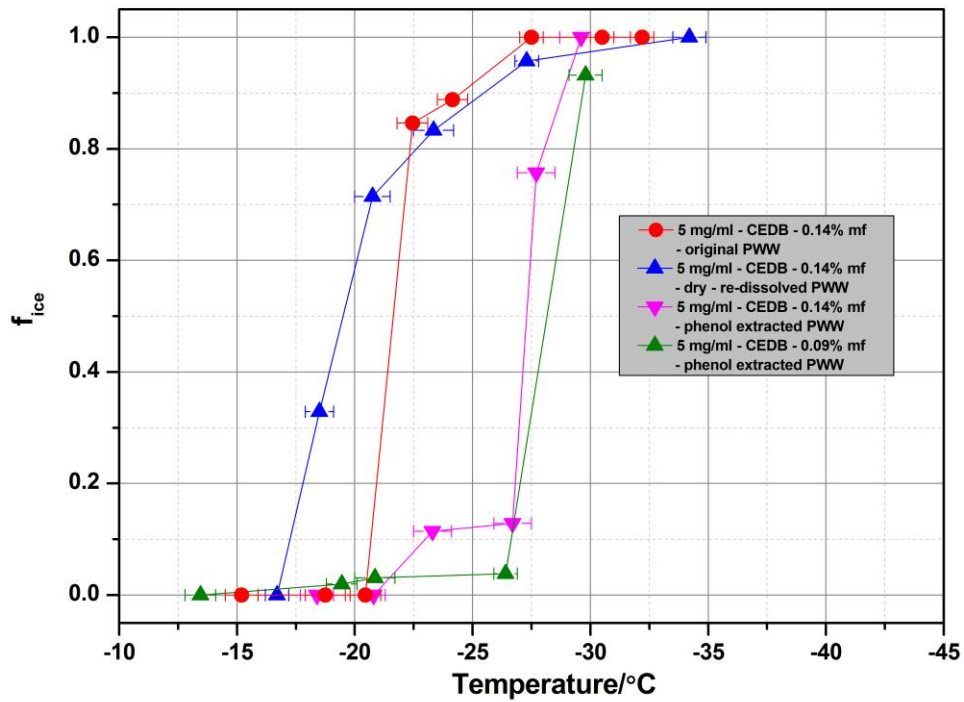
8

9

10

11

12



1

2 Figure 8. Freezing fraction of different kind of prearranged 5 mg ml<sup>-1</sup> birch PWW. Blue triangles: re-  
 3 dissolved PWW after drying out (mf=0.14%). Pink triangles: PWW extracted with phenol  
 4 (mf=0.14%). Olive triangles: PWW extracted with phenol (mf=0.09%). Red circles are the same data  
 5 as shown in figure 7.

6